Order-Disorder Structural Transitions in Mazes Built by Evaporating Drops

P. Panizza,* H. Algaba, M. Postic, G. Raffy, L. Courbin,† and F. Artzner
Univ Rennes, CNRS, IPR (Institut de Physique de Rennes)—UMR 6251, F-35000 Rennes, France

(Received 27 November 2017; published 15 August 2018)

We show that the evaporation of surfactant solutions confined in quasi-two-dimensional porous media creates micron-sized labyrinthine patterns composing the walls of a centimeter-sized maze. These walls are made of solid deposits formed during drying via a sequence of individual Haines jumps occurring at the pore scale. We rationalize this process driven by simple iterative rules with a cellular automaton that acts as a maze generator. This model well describes the formation dynamics and final structure of an experimental maze as functions of the wettability heterogeneities of a porous medium and its geometry. Also, our findings unveil the crucial role of two geometric dimensionless quantities that control the structural order of a maze.

DOI: 10.1103/PhysRevLett.121.078002

Evaporation is central to many industrial and natural processes [1]. Understanding the evaporation of liquid dispersions in porous media is important for various disciplines, e.g., soil physics [2,3] and civil engineering [4], and diverse processes such as the underground sequestration of CO_2 [5]. The key issue in most cases is to comprehend the creation, locus, and morphology of the solid deposits formed during drying. For instance, this topic is crucial in civil engineering, as salt weathering can cause severe damage to the built environment [6] and in material science as evaporation can help the design of novel smart materials [7]. Yet, the development of models for drying in porous media [8] and the proper description of the formation of deposits in such media [9,10] have remained elusive, as these tasks are generally challenging.

Here, we study the evaporation of surfactant solutions in porous media consisting of micron-sized cylindrical posts arranged on square or rectangular lattices. The manufactured evaporation devices are transparent and quasi-two-dimensional (2D). These two essential attributes allow us to precisely determine how and where solid deposits form during drying. As a fluid evaporates, labyrinthine patterns made of solid deposits form in the pores between adjacent posts. These "walls" compose a centimeter-sized structure that resembles a maze when drying ends. Labyrinthine patterns can also emerge in fluid-granular 2D flows [11] and other fluid systems submitted to an external field [12]. Phyllotaxy-inspired drying patterns can even be seen in suitably designed 2D porous media [13]. In our study, we show that the created walls result from the motion of unstable liquid-air menisci between neighboring posts, i.e., Haines jumps. Since these events are sequential and stochastic at the lattice scale and driven by iterative rules at the pore scale, we rationalize our results with a cellular automaton generating mazes. This model, which accounts for pore-scale heterogeneities of wettability known to impact drying in porous media [14,15], well describes the structure and formation dynamics of the observed mazes. For fixed wetting conditions, we show that the structural order of a maze is governed by only two geometric dimensionless quantities built with four key geometric parameters, the post radius, the lattice height, and interpost spacings.

An evaporation device consists of an assembly of posts sealed on top of a smooth solid (see Fig. 1), both surfaces being made of transparent polydimethylsiloxane (PDMS Sylgard 184, Dow Corning) using soft lithography [16]. The posts have a radius $R = 50$ μm and height $h = 20$–100 μm, the interpost spacings ℓ_1 and ℓ_2 being in the 150–250 μm range [Fig. 1(a)]. A drop of a deionized water surfactant (either SDS or Tween 20, concentration 5 cmc, Sigma-Aldrich) mixture is squeezed between textured and smooth surfaces and glue seals the sides of the device. The liquid then pervaporates [17,18] through the ceiling of the device placed in a container with constant temperature and humidity [Figs. 1(a) and 1(b)]. For the whole study, experimental and numerical drops begin to evaporate at the origin of time $t = 0$.

We use an inverted microscope (IX71, Olympus) and a camera (Eurocam) to record the evolution with time of the surface of an evaporating drop [Fig. 1(b); see Ref. [19] for further details of experimental methods]. In an evaporation device, the liquid-air interface consists of circular menisci connecting adjacent posts (see Figs. 1 and 2). As the surface of a drop decreases during drying, all menisci slowly recede with a decreasing radius of curvature R_c [Fig. 2(a)] until one of them becomes unstable and moves rapidly towards the liquid cell it contacts [see Fig. 2(b) and Video S1 in Ref. [19]); this is a Haines jump. As a result, new menisci or solid films or both are created at the three other edges of this cell [see Figs. 1(c)–2(b) defining the types of posts P_k and liquid cells N_k and illustrating the time evolution of these cells]. A wall is built between two neighboring posts when liquid gets trapped between the

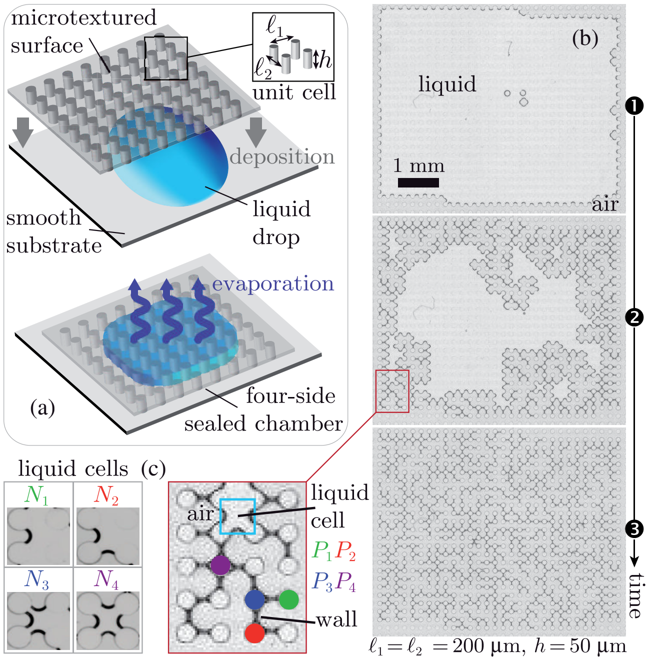

FIG. 1. (a) Schematics describing our experiment. (b) Top-view images of an evaporating drop initially comprising 665 liquid cells. The corresponding times are as follows: (1) $t = 0$ s, (2) $t = 8040$ s, and (3) $t = 26\,600$ s. (c) Images of the liquid cells N_k having k menisci and close-up view of the red box shown in (b) defining the posts P_k connected to k walls.

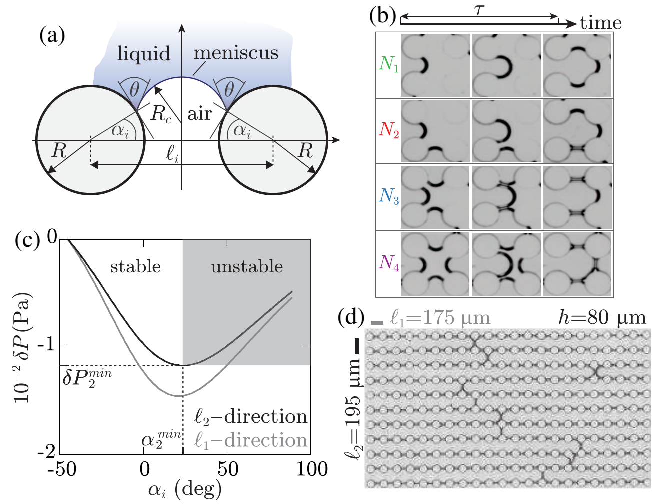

FIG. 2. (a) Top-view schematic of a meniscus connecting two adjacent posts defining geometric variables at play. (b) Photographs showing the four types of Haines jumps responsible for the time evolution of the liquid cells N_k and subsequent creation of walls. The loss of a cell N_k after a time τ produces $4 - k$ new menisci and $k - 1$ walls. (c) δP versus α_i for $\ell_1 = 175$ μm (gray) and $\ell_2 = 195$ μm (black). $\theta = 45°$ and $h = 80$ μm. The shaded area indicates the unstable region in the ℓ_2 direction. (d) Maze obtained with a rectangular lattice having geometrical parameters as in Fig. 2(c).

moving unstable meniscus merging with another meniscus located on one edge of the invaded liquid cell [Fig. 2(b)]. The evaporation of this liquid bridge creates a solid wall and possibly the crystallization of the dispersed phase as illustrated by x-ray scattering and scanning electron microscopy when a nanorod-based fluid system is used [20]. Our experiments show that (i) the contact angle θ that the liquid makes with PDMS is $\theta_m \leq \theta \leq \theta_M$ with typically $\theta_m \simeq 25°$ and $\theta_M \simeq 65°$ (see Fig. S1 and related discussion in Ref. [19]), (ii) each meniscus presents an axis of symmetry perpendicular to the line connecting the centers of the two posts it contacts [see Fig. 2(a)], and (iii) θ is unchanged during the motion of an unstable meniscus. Also revealed by our observations, the selection of unstable menisci is stochastic and their motions are sequential; i.e., they move one at a time. Hence, evaporation consists of successive Haines jumps separated by slowly evolving configurations (see Video S1 in Ref. [19]) until the process ends. The interconnected walls then form a centimeter-sized structure resembling a maze [Figs. 1(b) and 2(d)]. Being seen for different solute species (surfactants and colloids), these structures are inherent to the drying process. To study their formation dynamics and topology, we characterize the temporal evolution of $P_k(t)$ and $N_k(t)$ by processing images recorded during drying with custom-written C++ software.

An ℓ_i meniscus and an ℓ_i wall ($i = 1$ or 2) herein denote a meniscus and a wall connecting two adjacent posts with interpost spacing ℓ_i, respectively. Using geometry, one easily determines the radius of curvature $R_c = (\ell_i - 2R\cos\alpha_i)/[2\cos(\theta - \alpha_i)]$ of an ℓ_i meniscus with α_i the angle defining its position on the posts it contacts [see Fig. 2(a)]. The pressure at this meniscus is $P(\alpha_i, \theta, \ell_i, h) = P_o + \delta P$ with the ambient pressure (P_o) and Laplace pressure $\delta P = -\gamma(R_c{}^{-1} + 2h^{-1}\cos\theta)$, γ being the air-liquid surface tension [21]. We begin to rationalize our results by considering that θ is constant ($\theta = 45°$), as this simplified analysis helps us to understand the underlying physics of our experiment. Figure 2(c) shows that δP has a minimum $\delta P_i^{\min}$ for $\alpha_i = \alpha_i^{\min}$. Also, for any h, we find that $\delta P_2^{\min} \geq \delta P_1^{\min}$ when $\ell_2 \geq \ell_1$. As shown below in the case $\ell_2 > \ell_1$, these basic arguments are sufficient to explain the observed Haines jumps; note that similar arguments can be employed when $\ell_2 < \ell_1$.

Between two successive Haines jumps, δP is uniform so that α_1 and α_2 are small and different [see Fig. 2(c)]. As water evaporates, these two angles increase as δP decreases until it reaches the value $\delta P_2^{\min}$ [Fig. 2(c)]. Then, if a fluctuation causes an ℓ_i meniscus to move farther than the others, the pressure at this meniscus either decreases ($i = 1$) or increases ($i = 2$) [Fig. 2(c)]. Hence, the pressure gradient between this local pressure and that of other liquid cells induces a flow that either stabilizes ($i = 1$) or destabilizes ($i = 2$) the moving front. All ℓ_2 menisci are then potentially unstable. By contrast, all menisci are stable when $\delta P > \delta P_2^{\min}$ and $\alpha_i < \alpha_i^{\min}$ since δP decreases with α_i for both $i = 1$ and 2. Thus, all menisci should recede slowly at a speed set by the evaporation rate when $\delta P > \delta P_2^{\min}$ until a Haines jump occurs for $\delta P = \delta P_2^{\min}$. The motion of an unstable ℓ_2 meniscus induces a rapid transfer of liquid in the other cells which makes all other menisci advance. So, once a Haines jump is completed, the pressure $\delta P > \delta P_2^{\min}$ is uniform and all menisci are stable again. They recede slowly until another Haines jump occurs when $\delta P = \delta P_2^{\min}$.

Our analysis explains the observed evaporation characterized by a succession of individual Haines jumps. These stochastic events are periodic, their period τ being the time needed for a liquid cell to evaporate [see Fig. 2(b)]. As depicted in Fig. 2(b), a Haines jump yields the creation of new menisci or walls or both positioned along the edges of the invaded liquid cell according to simple rules. A wall is formed only when the unstable meniscus merges with another meniscus initially present on an edge of this liquid cell; a new meniscus is created otherwise. The final configuration of an invaded cell, thus, only depends its initial one observed just before the jump starts [Fig. 2(b)]. Within our approximation of constant angle θ, only ℓ_2 menisci are unstable during drying when $\ell_2 > \ell_1$. The structure of a maze should then be highly ordered with only one ℓ_2 wall formed per column of liquid cells in the ℓ_1 direction. The final structure shown in Fig. 2(d) concurs with this prediction that should neither depend on h nor the lattice anisotropy $\Delta\ell = \ell_2 - \ell_1$ when $\Delta\ell \neq 0$. For square lattices ($\Delta\ell = 0$), the whole picture is not altered. However, all ℓ_i menisci are potentially unstable in this case so that the fraction of ℓ_1 walls should be equal to that of ℓ_2 walls. This is qualitatively confirmed by the final structure of the maze shown in Fig. 1(b).

To validate our predictions quantitatively, we perform experiments in which we vary $\Delta\ell$ and h for a fixed ℓ_1. As predicted, the same number of walls is found in the two directions of the lattice for any h when $\Delta\ell = 0$, and the fraction of ℓ_2 walls is close to 0 when $\Delta\ell > 20$ μm [see Fig. 3(a)]. Unexpectedly, however, a large (≈0.1–0.4) fraction of ℓ_2 walls is found experimentally for intermediate $\Delta\ell$ at any h [Fig. 3(a)]; this fraction decreases with increasing $\Delta\ell$ (at fixed h) and h (for a given $\Delta\ell$).

Although our simple analysis based on a unique contact angle helps us to understand some results, it fails to explain the existence of unstable ℓ_1 menisci yielding the finite fraction of ℓ_2 walls seen for intermediate $\Delta\ell$. To that end, the contact angle is $\theta_m \leq \theta \leq \theta_M$ for the remainder of the study. For this problem driven by the iteration of simple rules, we develop a cellular automaton that acts as a maze generator to rationalize our experiments. This numerical model proceeds as follows. Each pore of a lattice is filled with either liquid or air and menisci connect the two types of cells. At each time step of the algorithm, we count the number M_i of ℓ_i menisci, we index their positions for both

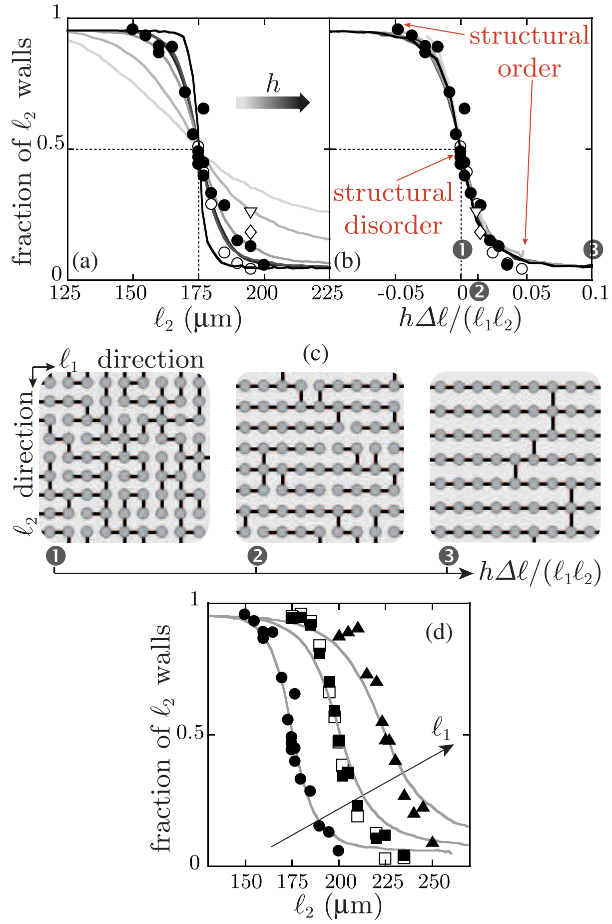

FIG. 3. (a) Experimental fraction of ℓ_2 walls vs ℓ_2 for $\ell_1 = 175$ μm and four post heights h: 20 μm (▿), 25 μm (⋄), 50 μm (•), and 80 μm (∘). The lines correspond to our model with $\theta_m = 25°$ and $\theta_M = 65°$. As indicated by the arrow, the shades of gray of the lines stand for different h varying from the lightest gray for the smallest post (10 μm) to black for the tallest one (200 μm) with intermediate values 20, 50, 80 and 100 μm. (b) Data shown in Fig. 3(a) vs $h\Delta\ell/(\ell_1\ell_2)$. (c) Close-up views of a few tens of pores depicting the final numerical structures for different $h\Delta\ell/(\ell_1\ell_2)$; when a simulation starts, a drop comprises 400 liquid cells. (d) Fractions of ℓ_2 walls vs ℓ_2 for $h = 50$ μm and different ℓ_1: 175 μm (•), 200 μm (■,□), and 225 μm (▲). The three lines are the outcomes of the cellular automaton for the water-SDS mixture with θ_m and θ_M as in Fig. 3(a). The open squares denote experiments conducted with the water-Tween 20 mixture.

$i = 1$ or 2 with an integer $1 \leq j_i \leq M_i$, and we randomly select a contact angle $\theta_m \leq \theta_{j_i} \leq \theta_M$ for each of them [22]. At each ℓ_i meniscus, the excess pressure in the liquid is now $\delta P(\theta_{j_i}, \alpha_i, \ell_i, h)$. Similar to our previous analysis assuming a constant angle [see Fig. 2(b)], as menisci move slowly between two Haines jumps, δP is uniform and decreases until it reaches the minimum value $\delta P_i^{\min}(\theta_{j_i}, \ell_i, h) = \min[\delta P(\theta_{j_i}, \alpha_i, \ell_i, h)]$ of the pressure profile at one meniscus. This minimum being the largest of all pressure profiles, the identified meniscus is unstable, and

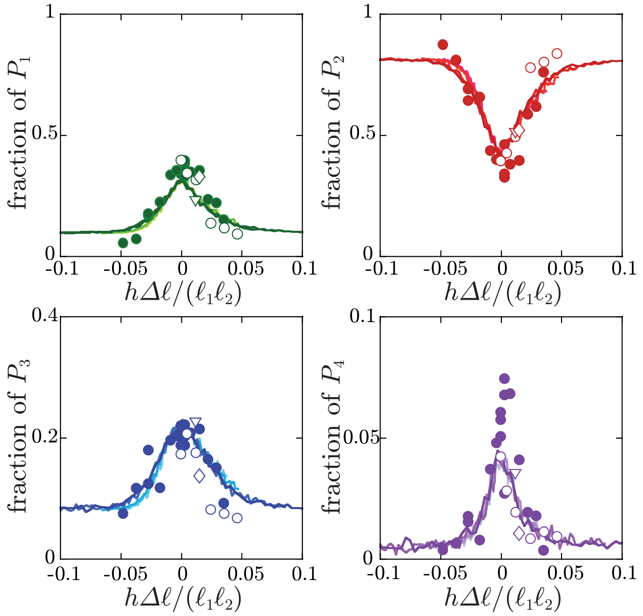

FIG. 4. Final fractions of P_k vs $h\Delta\ell/(\ell_1\ell_2)$ for $\ell_1 = 175$ μm ($\ell_1/R = 3.5$) and four post heights. The symbols are identical to those of Fig. 3(a). The lines are the outcomes of the cellular automaton with $\theta_m = 25°$ and $\theta_M = 65°$; the shades of color of the lines stand for the four heights varying from the lightest shade for the smallest post to the darkest shade for the tallest post.

the algorithm makes it invade its neighboring cell according to the rules depicted in Fig. 2(b).

To compare the model predictions with experiments, the initial shape of a squeezed drop and time step τ used in the simulations match the experimental ones. As shown in Fig. 3(a), the model accounting for wettability heterogeneities captures quantitatively well the experimental features that our simple analysis with a unique contact angle θ failed to describe. This model indeed explains the nonzero fractions of ℓ_2 walls measured for $0 < \Delta\ell < 20$ μm, fractions that decrease with increasing both ℓ_2 (at fixed h) and h (at fixed ℓ_2).

Interestingly, experimental and numerical data collapse onto a master curve when plotted as a function of $h\Delta\ell/(\ell_1\ell_2)$ [Fig. 3(b)]. Apart from the length scales involved in the numerator of this dimensionless quantity, it may be noted that this expression $[\propto 1/(\ell_1\ell_2)]$ is similar to that of the wetted solid fraction of posts by a drop suspended on a rectangular array of posts [23]; in Ref. [19], we discuss the physical origin of this quantity in further detail. The structural order of a maze appears to be an increasing function of this parameter, as illustrated by the numerical mazes shown in Fig. 3(c). In addition, our model predicts well the variations of the fraction of ℓ_2 walls when ℓ_1 varies and final values of the fractions of P_k (see Fig. 4), and our experiments seem to be independent of the nature of the surfactant [see Fig. 3(d)]. In our study with four geometric parameters (h, ℓ_1, ℓ_2, R) at play, Fig. 3(b) reveals the governing dimensionless quantity $h\Delta\ell/(\ell_1\ell_2)$. R and ℓ_1 being constant in this figure, ℓ_1/R is another governing quantity (see Fig. S2 and a discussion of these quantities in Ref. [19]). Hence, the data reported for different ℓ_1/R in Fig. 3(d) cannot collapse onto a master curve as a function of $h\Delta\ell/(\ell_1\ell_2)$ (see, also, Fig. S2(b) in Ref. [19]). As shown in Ref. [19], our model also captures the formation dynamics of a maze, i.e., the temporal variations of $P_k(t)$ and $N_k(t)$, for square (Fig. S3 and Video S2 in Ref. [19]) and rectangular (Fig. S4 and Video S3 in Ref. [19]) lattices; as illustrated in Fig. S4 in Ref. [19], our analysis does not capture the details of these variations because of the stochastic nature of the Haines jumps at the origin of the formation of a maze.

To conclude, studying the evaporation of surfactant solutions in transparent 2D porous media, we unravel the mechanisms governing the formation of solid deposits in the micron-sized pores, these deposits composing the walls of a centimeter-sized maze. Interestingly, two posts of a maze are connected by one path only; these mazes are called "perfect," and they are equivalent to a tree in graph theory. We model our findings with a cellular automaton accounting for wettability heterogeneities and acting as a maze generator that captures the structure of a created maze and its formation dynamics. Also, our findings unveil two geometrical dimensionless quantities that allow for a fine-tuning of the structural order of a maze. These results could help the design of multiscale materials using evaporation as a route for controlled self-assembly. In particular, the design rules described here could find applications in flexible electronics as they offer possibilities for tailoring microwire networks.

This work was partially funded by Grant No. 2013601 obtained from Direction Générale de l'Armement.

*pascal.panizza@univ-rennes1.fr
†laurent.courbin@univ-rennes1.fr

[1] W. Brutsaert, *Evaporation into the Atmosphere: Theory, History and Applications* (Springer, Dordrecht, 1982).
[2] A. S. Goudie and H. A. Viles, *Salt Weathering Hazards* (Wiley, London, 1997).
[3] U. Nachshon, N. Weisbrod, M. I. Dragila, and A. Grader, Combined evaporation and salt precipitation in homogeneous and heterogeneous porous media, Water Resour. Res. **47**, W03513 (2011).
[4] F. G. Bell, Durability of carbonate rock as building stone with comments on its preservation, Environ. Geol. **21**, 187 (1993).
[5] Y. Peysson, M. Fleury, and V. Blasquez-Pascual, Drying rate measurements in convection- and diffusion-driven conditions on a shaly sandstone using nuclear magnetic resonance, Transp. Porous Media **90**, 1001 (2011).
[6] N. Shahidzadeh-Bonn, J. Desarnaud, F. Bertrand, X. Chateau, and D. Bonn, Damage in porous media due to salt crystallization, Phys. Rev. E **81**, 066110 (2010).

[7] I. U. Vakarelski, D. Y. C. Chan, T. Nonoguchi, H. Shinto, and K. Higashitani, Assembly of Gold Nanoparticles into Microwire Networks Induced by Drying Liquid Bridges, Phys. Rev. Lett. **102**, 058303 (2009).

[8] For a review on models of drying in porous media, see, for instance, M. Prat, Recent advances in pore-scale models for drying of porous media, Chem. Eng. J. (London) **86**, 153 (2002).

[9] R. Du and H. A. Stone, Evaporatively controlled growth of salt trees, Phys. Rev. E **53**, 1994 (1996).

[10] S. Veran-Tissoires, M. Marcoux, and M. Prat, Discrete Salt Crystallization at the Surface of a Porous Medium, Phys. Rev. Lett. **108**, 054502 (2012).

[11] B. Sandnes, H. A. Knudsen, K. J. Måløy, and E. G. Flekkøy, Labyrinth Patterns in Conned Granular-Fluid Systems, Phys. Rev. Lett. **99**, 038001 (2007).

[12] R. E. Rosensweig, M. Zhan, and R. Shumovich, Labyrinthine instability in magnetic and dielectric fluids, J. Magn. Magn. Mater. **39**, 127 (1983).

[13] C. Chen, P. Duru, P. Joseph, S. Geoffroy, and M. Prat, Control of evaporation by geometry in capillary structures. From conned pillar arrays in a gap radial gradient to phyllotaxy-inspired geometry, Sci. Rep. **7**, 15110 (2017).

[14] H. Chraïbi, M. Prat, and O. Chapuis, Influence of contact angle on slow evaporation in two-dimensional porous media, Phys. Rev. E **79**, 026313 (2009).

[15] O. Borgman, P. Fantinel, W. Lühder, L. Goehring, and R. Holtzman, Impact of spatially correlated porescale heterogeneity on drying porous media, Water Resour. Res. **53**, 5645 (2017).

[16] D. C. Duffy, J. Cooper McDonald, O. J. A. Schueller, and G. M. Whitesides, Rapid prototyping of microfluidic systems in poly(dimethylsiloxane), Anal. Chem. **70**, 4974 (1998).

[17] J. B. Salmon and J. Leng, Application of microevaporators to dynamic exploration of the phase diagram, J. Appl. Phys. **107**, 084905 (2010).

[18] N. Ziane and J. B. Salmon, Solidication of a charged colloidal dispersion investigated using microfluidic pervaporation, Langmuir **31**, 7943 (2015).

[19] See Supplemental Material at http://link.aps.org/supplemental/10.1103/PhysRevLett.121.078002 for details of experimental methods, typical distributions of contact angles, a brief discussion on governing parameters, two figures comparing experimental, and numerical formation dynamics for rectangular and square lattices and three videos. Video S1 illustrates experimental Haines jumps and the resulting formation of walls. Videos S2 and S3 show that the experimental structures of a maze compare well to numerical predictions for both kinds of lattices.

[20] C. Hamon, M. Postic, E. Mazari, T. Bizien, C. Dupuis, P. Even-Hernandez, A. Jimenez, L. Courbin, C. Gosse, F. Artzner, and V. Marchi-Artzner, Three-dimensional self-assembling of gold nanorods with controlled macroscopic shape and local smectic B order, ACS Nano **6**, 4137 (2012).

[21] The surface tensions determined by pendant drop tensiometry are 35 and 36 $\mathrm{mN\,m^{-1}}$ for the SDS-based system and the Tween 20-based one, respectively.

[22] We consider a typical length scale of wettability heterogeneities given by that of a meniscus and a rectangular distribution of contact angles θ for the sake of simplicity.

[23] A. Gauthier, M. Rivetti, J. Teisseire, and E. Barthel, Role of Kinks in the Dynamics of Contact Lines Receding on Superhydrophobic Surfaces, Phys. Rev. Lett. **110**, 046101 (2013).